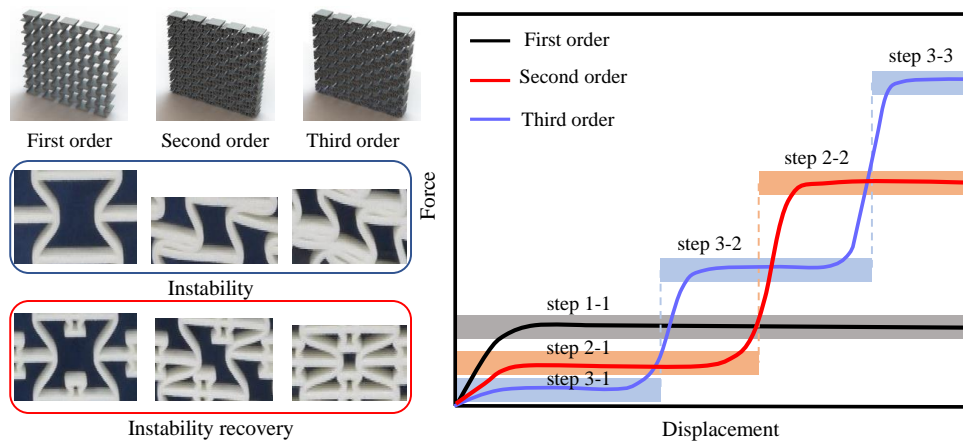# Graphical Abstract

A multi-step auxetic metamaterial with instability regulation

Penghui Yu[a], Peijie Zhang[a], Qingxiang Ji[a], Fan Yang[a], Xiaojun Tan[b], Xueyan Chen[a], Huifeng Tan[a], Vincent Laude[c], Muamer Kadic[c]

Highlights

A multi-step auxetic metamaterial with instability regulation

Penghui Yu[a], Peijie Zhang[a], Qingxiang Ji[a], Fan Yang[a], Xiaojun Tan[b], Xueyan Chen[a], Huifeng Tan[a], Vincent Laude[c], Muamer Kadic[c]

- We propose a multi-step auxetic metamaterial design paradigm, incorporating a series of incrementally scaled-down structures into a re-entrant framework.

- This design enables instability regulation and multi-step deformation capabilities while preserving auxetic behavior, even under significant strain.

- Such multi-step metamaterials exhibit excellent properties, including tailored multi-phase compression modulus and strength, along with an enhanced energy absorption capacity that is as large as 2.1 times that of the original auxetic metamaterial.

- At high relative density, specific energy absorption of design S-1/5A stands out, highlighting the success of the recoverable buckling mechanism.

A multi-step auxetic metamaterial with instability regulation

Penghui Yu[a], Peijie Zhang[a], Qingxiang Ji[a], Fan Yang[a], Xiaojun Tan[b], Xueyan Chen[a*], Huifeng Tan[a*], Vincent Laude[c], Muamer Kadic[c*]

[a] *National Key Laboratory of Science and Technology on Advanced Composites in Special Environments, Harbin Institute of Technology, 92 Xidazhi Street, Harbin, 150001, PR China*
[b] *School of Civil Aviation, Northwestern Polytechnical University, Xi'an 710072, PR China*
[c] *Université de Franche-Comté, CNRS, Institut FEMTO-ST, 25000 Besançon, France*

Abstract

A stable deformation mode is highly desired for mechanical metamaterials, especially when coupled with a negative Poisson's ratio. However, such metamaterials often face challenges in terms of scalability toward large deformation or strain. In response, we propose a multi-step auxetic metamaterial design paradigm, incorporating a series of incrementally scaled-down structures into a re-entrant framework. This design enables instability regulation and multi-step deformation capabilities while preserving auxetic behavior, even under significant strain. Such multi-step metamaterials exhibit excellent properties, including tailored multi-phase compression modulus and strength, along with an enhanced energy absorption capacity that is as large as 2.1 times that of the original auxetic metamaterial. Experiments and simulations demonstrate that the deformation mechanism and compression response of the proposed multi-step auxetics are strongly influenced by the reduction factor and the order of the inner structure. A particularly intriguing observation is that the incorporation of embedded microstructures can restore stable deformation, even in the presence of significant initial instability, particularly with a reduction factor of 1/5. At high relative density, its specific energy absorption stands out favorably compared to other configurations, highlighting the success of the recoverable buckling mechanism. This work paves the way for designing multi-step mechanical metamaterials for use in impact resistance and body protection.

Keywords:
Auxetics, Mechanical metamaterial, Lightweight structure, Multi-step deformation, Tailored stability

1. Introduction

Mechanical metamaterials, with their meticulously engineered periodic microstructures, display an extensive array of mechanical properties, including programmable deformations[1, 2, 3, 4], controlled Poisson's ratio[5, 6, 7, 8, 9], high specific stiffness[10, 11, 12], high specific

---

strength[13, 14], high energy absorption[15, 16, 17], and reusable shock-absorbing capacity[18, 19]. These mechanical properties are primarily influenced by structural topology, geometrical parameters, and the inherent characteristics of base materials[20, 21, 22, 23].

Auxetics are a distinctive class of mechanical metamaterials characterized by a negative Poisson's ratio, which contract (expand) transversely when compressed (stretched) longitudinally. This unconventional behavior provides them with enhanced mechanical properties[24, 25], including shear and indentation resistance[26, 27], fracture toughness[28], energy absorption capabilities[29, 30], and wave propagation characteristics[31, 32], when compared to mechanical metamaterials with a positive Poisson's ratio. Auxetic mechanical materials thus have garnered significant interest across diverse engineering disciplines, spanning civil and military sectors[33], automotive engineering[34], aerospace devices[35, 36], medical implants[37], flexible electronics[38], and more.

Pioneering this domain, Lakes introduced a 3D artificial auxetic foam where the ribs of each cell were designed to protrude inward permanently[39]. Later, Evans et al. defined the notion of auxeticity[40]. Grima et al. expanded the auxetic materials repertoire by incorporating a mechanism composed of rotating rigid units, encompassing rotating squares[41, 42], rectangles[43], triangles[44], and variously sized squares and rectangles[45]. Since then, a myriad of auxetic materials has been conceived, employing diverse deformation mechanisms such as re-entrant structures[46, 47, 48], chiral structures[49, 50, 51], rotating polygon structures[8, 52], perforated plate structures[53, 54], and other structures[55, 56]. Recent breakthroughs in additive manufacturing allow for the creation of auxetic mechanical materials across multiple length scales employing a diverse range of base materials[57, 5, 6].

Re-entrant structures hold a pivotal position within the auxetic family. The earliest example of 2D re-entrant honeycombs, achieved by incorporating a negative angle into the inclined member of a standard honeycomb structure, was introduced by Gibson et al. in 1982[46]. Building on this foundation, subsequent research delved into the elastic constants of these structures, analyzing honeycomb cell deformations like flexure, stretching, and hinging[58]. A noteworthy theoretical method was proposed, predicated on comparing strain energies at both the macro and micro scales, aiming to predict the effective properties of 2D re-entrant structures[59]. For minimizing stress concentration around junctions, dynamic in-plane responses and multi-objective optimization of re-entrant structures, shaped by a sinusoidal curve, were obtained[60]. By merging the re-entrant honeycomb design with hexagonal patterns, a new hybrid honeycomb structure was discerned. This structure boasts augmented stiffness, adjustable auxeticity, and exhibits negative thermal expansion[61]. Additionally, Zhang et al. conducted a comprehensive study on the post-yield behavior of re-entrant hexagonal honeycombs under tension, using both analytical and numerical approaches[62].

Generally, at low relative densities, these metamaterials exhibit global instability when subjected to large deformations, which in turn affects their mechanical properties[63, 64, 65, 66]. To address this challenge, numerous scholars have embarked on structural optimization designs rooted in the traditional concave structure with a negative Poisson's ratio. Innovations such as the inclusion of embedded microstructures[67, 68] and the development of hierarchical designs[69, 70] have been explored to fortify their mechanical response. Nonetheless, these strategies introduce new complications, including increased structural mass and potential shifts from the foundational negative Poisson's ratio attributes of the material. Consequently, there is a pressing demand to devise a novel optimization approach that not only bolsters the nonlinear stability of re-entrant auxetic structures but also amplifies their energy absorption capabilities.

Multi-step deformation structures can impart unique and significant mechanical properties.

2

Coulais et al. introduced a metamaterial capable of multi-step deformation, achieved via structural reconfiguration guided by a rotating mechanism, thereby negating the need for external sensing and control[1]. This underlying mechanism can also serve as a foundation for designing other multi-step metamaterials[71, 72, 73]. Building upon this idea, Meng et al. introduced an innovative multi-step deformation structure that seamlessly combines sequential cell deformation with Euler buckling[74]. In a different study, Jiang et al. examined the dual plateau characteristics of the re-entrant auxetic structure in its concave orientation[75]. Meanwhile, Dudek et al. presented a micro-scale mechanical metamaterial featuring tunable extreme auxeticity and phononic band gaps, facilitated by structural reconfiguration[52]. Collectively, muti-step deformation mechanisms demonstrate remarkable potential in the realm of deformation control.

Stemming from these insights, we propose in this work a novel class of re-entrant auxetic metamaterial, integrated with microstructures of varying reduction ratios, specifically designed for energy absorption and instability regulation. The effects of geometrical parameters on the effective mechanical properties are analyzed using numerical simulations and experiments. Results show that the proposed structure not only offers modifiable multi-step deformation capabilities but also spans a broad range of auxetic behaviors. A particularly intriguing observation is that certain mechanical metamaterials, when embedded with microstructures of a distinct size, have the capacity to display a unique "instability recovery" phenomenon. Compared to the conventional re-entrant auxetic materials, the designed metamaterials have a specific energy absorption about 2.1 times as large.

2. Metamaterial design

We first outline a comprehensive design strategy that involves embedding a series of incrementally scaled-down structures into a 2D auxetic re-entrant framework (Fig. 1a and b). This approach aims to achieve controlled multi-step deformation behavior while also managing instabilities.

2.1. Design strategy

The design is based on a 2D re-entrant sinusoidal auxetic structure. It undergoes contraction by a factor α, followed by embedding at the top and bottom to create a second-order deformation structure. Subsequently, further scaling down by α and embedding within inner layers yields a third-order deformation structure. The core mechanism in this study involves converting the overall load into multiple deformation paths through sequential layer deformation within the unit cell (Fig. 1c). To demonstrate the general deformation mechanism, we subject numerically mechanical metamaterials consisting of 2×2 units to uniaxial compression under periodic boundary conditions (Fig. 1d). In terms of geometry, the embedding of the internal microstructure initiates deformation through the outer layer of the unit cell during the compression process. As the outer layer of the unit cell comes into contact with the internal microstructure, it drives the inner microstructure to deform (Fig. 1e), resulting in a multi-step deformation mechanism. Note that, in principle, the proposed design concept can be further extended to create metamaterials with n-step deformation.

Nonlinear stability is another significant concern in mechanical metamaterial. Conventionally, for first-order auxetics with low relative density, deformation behaviors at large strains are often unstable and thus need to be controlled (Fig. 1f). Unlike first-order auxetics, which typically buckle under axial compression, second-order auxetics, along with their embedding structures, have the capability to transform from an unstable stage to a stable stage (Fig. 1f). Certainly,
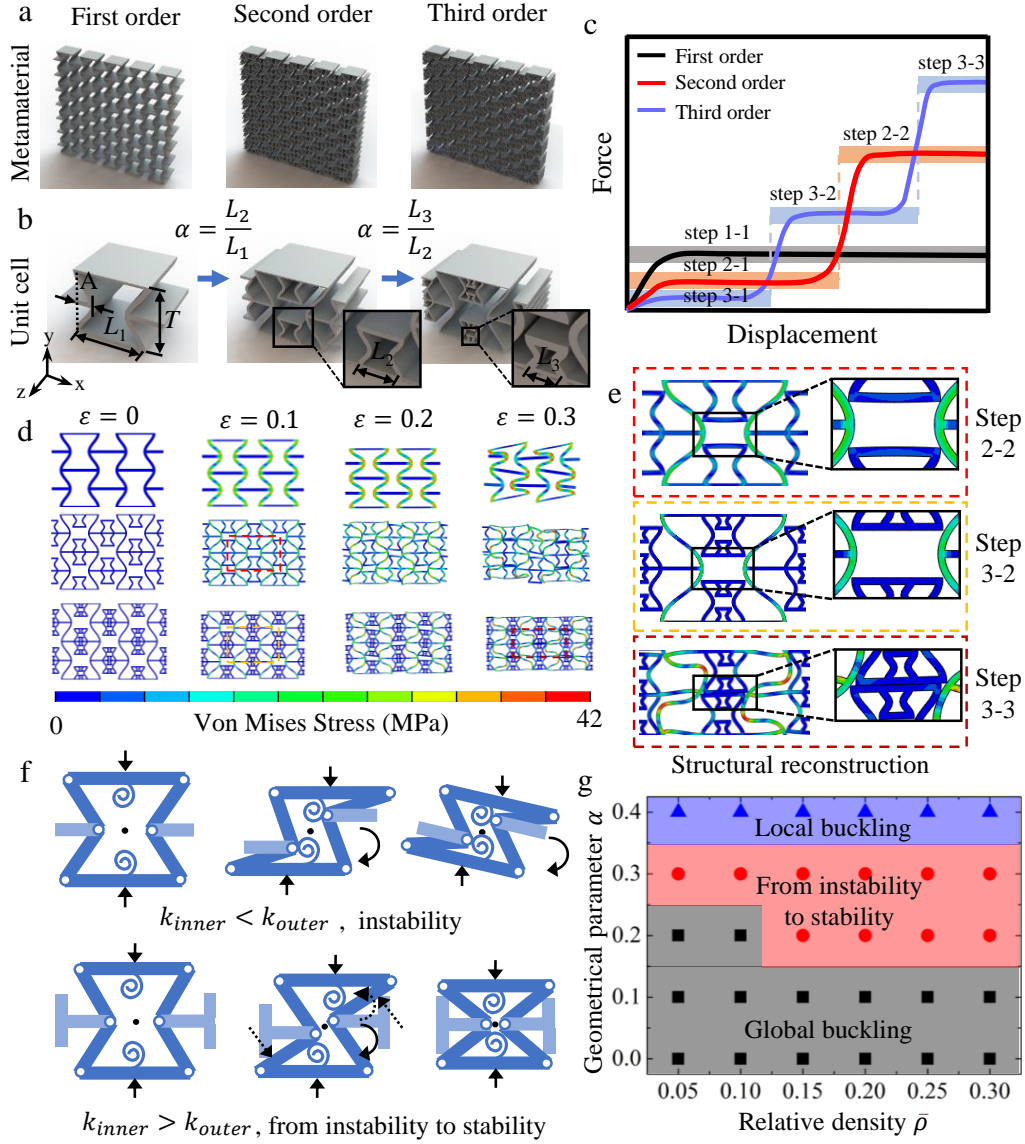
Figure 1: Design concepts of multi-step auxetic metamaterials. Schematics of (a) the first-order conventional auxetic metamaterial, the high-order optimal multi-step auxetic metamaterials, and (b) their corresponding representative unit cells. (c) Force-displacement curves for the auxetic materials show the multi-step mechanical response. (d) Uniaxial compression simulations for the auxetic materials with periodic boundary conditions applied, (e) accompanied by zoom-in views of structural reconstructions within these multi-step auxetic materials under a specific applied strain, illustrate the deformation mechanism. (f) Conventional buckling mechanism is shown versus the unusual instability transition mechanism of multi-step auxetics. In this representation, the inner scaled-down amended structures are symbolized as simplified spirals. (g) The deformation modes of second-order auxetics vary with relative densities and reduction ratio, exhibiting three types: destabilization, recovery after destabilization, and destabilization after stabilization. The geometrical parameter α and relative density $\bar{\rho}$ are defined in the text, Section 2.1.

the deformation path can also be carefully tailored to suppress or even avoid buckling behavior. Here, we numerically investigate the effects of reduction factor α and relative density $\bar{\rho}$ on the desired deformation mode. Utilizing 3×5 numerical models, we specially explore geometrical parameters ranging from α=0 to 0.4 and $\bar{\rho}$ from 0.05 to 0.3 (Fig. 1g). When α is constrained to values no greater than 0.1, the size of the embedded micro-structure results in an insufficient impact on regulating instability. In this scenario, the deformation modes of auxetics are predominantly governed by buckling. Upon increasing α to 0.2 and maintaining $\bar{\rho}$ within the confines of 0.1, the embedded micro-structures, characterized by thin thicknesses, contribute a low equivalent stiffness. Consequently, they prove ineffective in resisting the rotational deformation of the outer structure, and the deformation rule persists unchanged. However, a noteworthy transformation occurs when α is further elevated to 0.3 or when $\bar{\rho}$ exceeds 0.1. above these thresholds, the embedded micro-structures exhibit heightened strength, effectively countering the rotational deformation of the outer structure. Subsequently, the overall structure undergoes a pronounced recovery, gradually returning to a stable stage after experiencing nonlinear instability. This signifies a critical transition where the embedded micro-structures become robust enough to decisively influence the structural response. At an α value of 0.4, the embedded microstructures assume a larger size and undergo reconstruction before the structure experiences destabilization. This preemptive reconstruction serves to stabilize the deformation at the initial stage, mitigating the destabilization process. Nevertheless, as the structure progresses, it gradually becomes destabilized at a later stage. These mechanisms enable the structure to withstand higher loads and significantly mitigates the risk of the original re-entrant auxetic structure experiencing instability buckling during compression. Consequently, the designed structures can serve as a stable energy-absorbing element.

2.2. Relative density

Figure S1 illustrates the geometry of the first-order auxetic unit cell along with its associated geometric parameters. The first-order re-entrant auxetic structure exhibits a sinusoidal curve shape on the side of the unit cell with the following expression:

$$y = A \cos\left(\frac{2\pi}{T}x\right). \tag{1}$$

The unit cell dimensions in the x and y directions are:

$$L_x = 4(L - A), \; L_y = T, \tag{2}$$

where A represents the amplitude of the sine curve, L corresponds to half the length of the horizontal part of the single cell, and T stands for the period of the sine curve. The unit cell size in the z direction is denoted as L_z, and the layer thickness is represented by t.

Relative density $\bar{\rho}$ is a crucial factor in mechanical metamaterials, primarily used to manage their mass. It is defined as the ratio of the actual volume occupied by the mechanical metamaterials to the volume of the overall mechanical metamaterials. The relative density of the first-order auxetic metamaterial, determined by the ratio of the solid area of the structural cell (A_s) to its total cross-sectional area (A_{total}), can be expressed as:

$$\bar{\rho}_1 = \frac{A_s}{A_{\text{total}}} = \frac{(S + 2L)t - t^2}{2T(L - A)}, \tag{3}$$

5

where the length of the sinusoidal part of the side of the unit cell is $S = \int_{-\frac{T}{2}}^{\frac{T}{2}} \sqrt{1 + (\frac{2\pi A}{T} \sin(\frac{2\pi}{T}x))^2} dx$. Likewise, expressions for the relative densities of second-order, third-order and even n-order structures can also be derived:

$$\bar{\rho}_2 = \frac{(S + 2L)t + 4\alpha t(S + L) - 3t^2}{2T(L - A)}, \tag{4}$$

$$\bar{\rho}_3 = \frac{(S + 2L)t + 4\alpha t(S + L)(1 + 2\alpha) - 5t^2}{2T(L - A)}, \tag{5}$$

and

$$\bar{\rho}_n = \frac{(S + 2L)t + 4\alpha t(S + L)\frac{(2\alpha)^{n-1}-1}{2\alpha-1} - (2n - 1)t^2}{2T(L - A)}, \quad 0 \le \alpha < \frac{1}{2}. \tag{6}$$

Here, for the sake of illustration, we consider an example with amplitude $A = L/4$ and period $T = 2L$. With these values, the expression for relative density can be reformulated as follows:

$$\bar{\rho}_1 = \frac{t}{3L}\left(\frac{S}{L} + 2 - \frac{t}{L}\right), \tag{7}$$

$$\bar{\rho}_2 = \frac{t}{3L}\left(\frac{S}{L} + 2 - \frac{3t}{L} + 4\alpha\frac{S}{L} + 1\right), \tag{8}$$

and

$$\bar{\rho}_3 = \frac{t}{3L}\left(\frac{S}{L} + 2 - \frac{5t}{L} + 4\alpha(1 + 2\alpha)t\left(\frac{S}{L} + 1\right)\right). \tag{9}$$

These equations are employed to equate the mass among various orders of auxetic metamaterials.

3. Experiments

We conducted uniaxial tensile experiments on polymer sheets to establish the constitutive relation of the base material. Additionally, we performed compression tests on auxetics to demonstrate their substantial deformation behavior and validate the accuracy of the simulation results. Building on the numerical results, reduction ratios within the transform zone of 0.2 to 0.4 were selected, specifically 1/3, 1/4, and 1/5.

3.1. Fabrication of samples

We designed multi-step auxetic metamaterials and compared them to the original auxetic (OA) metamaterials. Samples were fabricated using selective laser sintering (SLS) technology on a commercial 3D printer (EOS model P110). The base material employed was PA 2200, and the fabrication process utilized a laser power of 30 W and a scanning speed of 5 m/s. The operational temperature was maintained at 190°C, and the layer thickness was set at 0.06 mm. After manufacturing, an ultrasonic bath was used to remove any unsintered powder residue. Each specimen comprises 5×7 unit cells. Six configurations at a relative density of 0.2 were investigated. The design dimensions for configuration T-1/3A are 200 mm $\times$ 186.69 mm $\times$ 26.67 mm, whereas for the other configurations they are 150 mm $\times$ 140 mm $\times$ 20 mm. The

OA configuration has a wall thickness of 1.48 mm. Additionally, five high-order configurations were selected to examine the impact of the inner structure and the hierarchical distribution on mechanical properties. The second-order auxetic configuration with $\alpha = 1/5$ (S-1/5A) has a wall thickness of 0.9 mm. Similarly, other second-order auxetic configurations are abbreviated as S-1/4A ($\alpha = 1/4$) and S-1/3A ($\alpha = 1/3$). Their corresponding wall thicknesses are 0.82 mm and 0.72 mm, respectively. For third-order auxetic configurations, only $\bar{\rho} = 0.2$ is considered here due to the limitation of the inner structure. The wall thicknesses of configurations T-1/4A and T-1/3A are 0.74 mm and 0.72 mm, respectively. One sample was manufactured for uniaxial compression experiments for each configuration. Detailed geometrical parameters for the fabricated samples are summarized in Table 1. The maximum measured dimensions were within 1% of the designed values, and the maximum mass error between as-designed and measured samples was less than 9.5%.

Table 1: Measured dimensions and mass error of the printed specimens.

Type	Relative density	Direction 1 (mm)	Direction 2 (mm)	Direction 3 (mm)	Error on mass (%)
OA	0.2	149.39	140.46	20.16	3.5
S-1/5A	0.2	149.54	139.52	20.33	-2
S-1/4A	0.2	148.73	140.09	20.01	5
S-1/3A	0.2	149.59	140.77	19.84	9.5
T-1/4A	0.2	148.72	139.13	19.84	1.5
T-1/3A	0.2	198.46	185.47	26.45	0.5

3.2. Characterization of the base material

To obtain the mechanical properties of the base material, we fabricated five dog-bone specimens for tensile testing in accordance with ASTM 638 standards, using the same laser processing method employed for auxetic samples. The stress-strain curves (Fig. 2a) for these specimens were acquired through tensile tests conducted on the printed specimens using a 50 kN universal testing machine (INSTRON-5569) at room temperature, with a constant loading rate of 10^{-3} s^{-1}. The axial tensile strain was measured with a mechanically clamped extensometer. The average Young's modulus is about 1.27 GPa, and the 0.2% offset yield stress is about 25 MPa. The base material fractures at a strain of 0.2, and its corresponding strength is 40.7 MPa.

3.3. Experimental procedure

Compression experiments were conducted using an Instron machine equipped with a 50 kN load cell, operating at a nominal strain rate of 10^{-3} s^{-1}. During the experiment, specimens were centrally positioned on the loading device platen in the front and rear directions to prevent eccentric forces and out-of-plane instability, as shown in Fig. 2b. A preload force was applied to avoid slipping between the specimens and platens. The loading continued until the applied strain reached 0.6. An optical camera recorded the deformation process and was used to adjust the
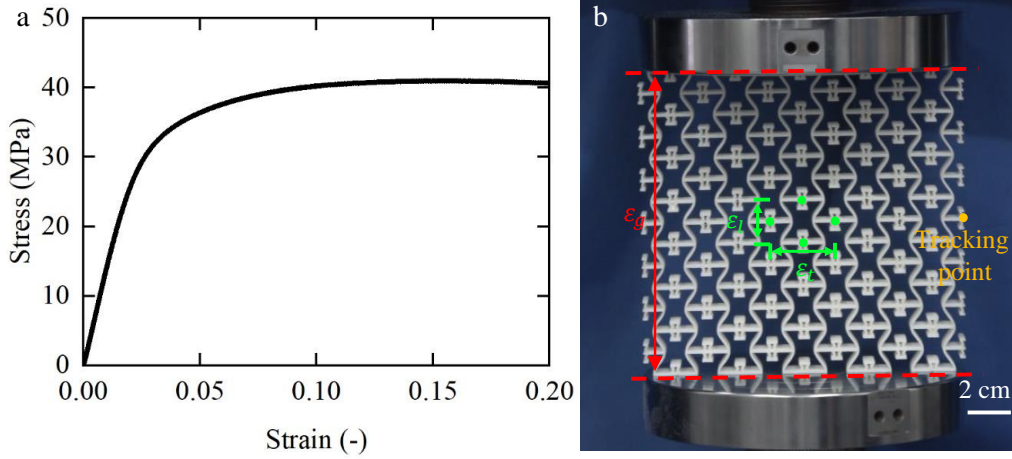
Figure 2: (a) Measured stress-strain curve of the base material. (b) Definition of reference points and lines for tracking local and global strains in the printed samples during the compression tests.

load and displacement curves through a digital image correlation algorithm [76], which provides sub-pixel resolution for tracking and analyzing displacement. To mitigate boundary effects, Poisson's ratio was calculated from the average longitudinal and transverse strain, measured at four reference points along the central row of auxetics. Similarly, the elastic modulus was calculated based on the longitudinal strain. For tracking the deformation path of the entire structure, one point was marked on the right side of the samples. Engineering stress and strain were determined by dividing the measured force and calibrated displacement by the cross-sectional area and height of specimen, respectively.

4. Numerical simulations

To determine the elastic mechanical properties of the first-order, second-order, and third-order auxetic structures, a series of unit cell models were constructed using the commercial software Abaqus. These models covered a range of reduction factors α from 1/5 to 1/3 and relative densities from 0.05 to 0.2. Due to their thin thickness, auxetic structures with low relative densities ($\bar{\rho}$=0.05) were built using the quadrilateral shell elements (type S4R of the Abaqus element library) following simpson's rule with 5 integration points across the thickness. For auxetic structures with high relative densities ($\bar{\rho} = 0.1, 0.15, 0.2$), first-order solid elements (type C3D8R) were used, with a minimum of four elements through the thickness. The T-1/4A unit cell has the highest number of mesh elements, approximately $1,746,800$. In all models, the unit cell geometrical dimensions are set to 30 mm × 20 mm × 20 mm. The corresponding wall thicknesses were adjusted with the relative density. We used an isotropic elasto-plastic model with isotropic hardening behavior to represent the mechanical properties of the constituent materials. The specific mechanical parameters are detailed in Fig. 2a, and the material Poisson's ratio is set to 0.4. Periodic boundary conditions are applied to unit cell models by matching mesh nodes on opposite planes with linear constraint equations. Young's modulus and effective Poisson's ratio were determined through elastic simulations with an applied strain of 10^{-4}.
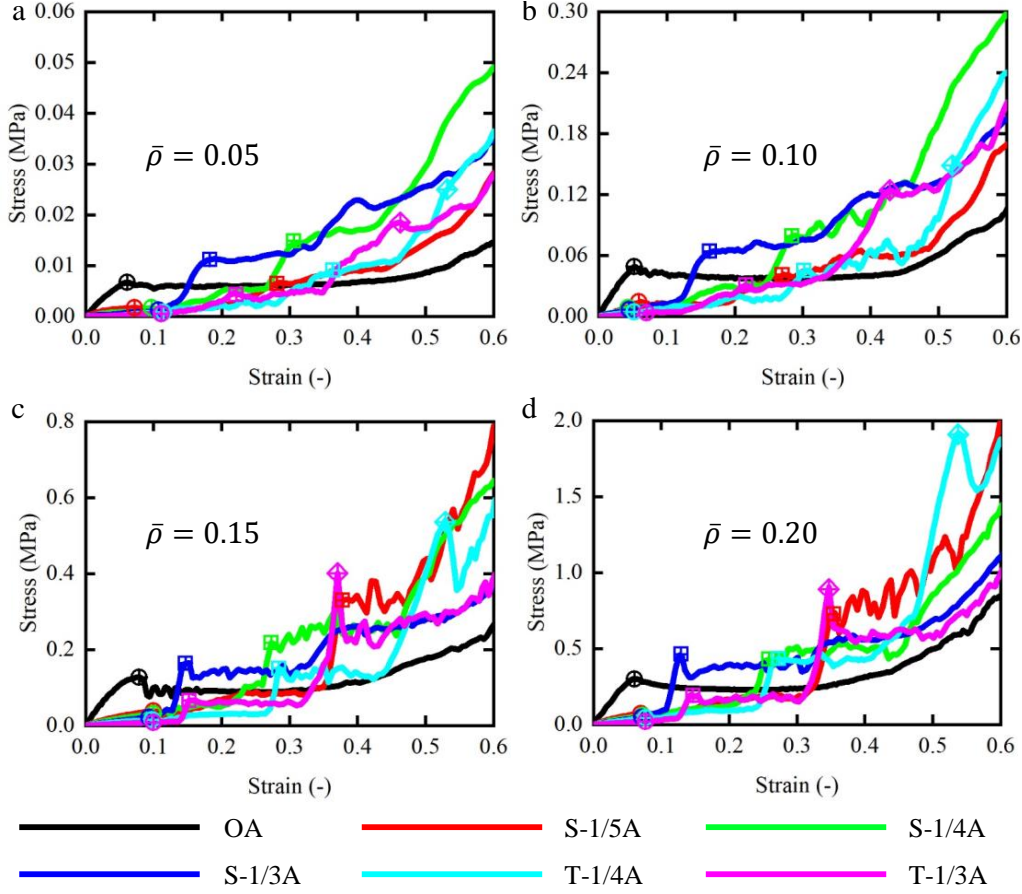
8

Figure 3: Nonlinear compressive response of six distinct auxetic configurations across a spectrum of relative densities, ranging from 0.05 to 0.2 at an interval of 0.05. In configuration names S-1/5A, S-1/4A, S-1/3A, T-1/4A, and T-1/3A, the fraction is the value of parameter α.

To explore the nonlinear mechanical behaviors of the first-order, second-order, and third-order auxetic structures, we generated numerical models consisting of 5×7 unit cells for all considered relative densities. The multi-cell models were meshed using either quadrilateral shell elements (type S4R) or planar elements (type CPS4R), depending on the relative density. The largest numerical model contained approximately 2.2 million mesh elements to ensure mesh accuracy. The numerical model was positioned between two analytical rigid surfaces. The bottom plate was held fixed, while the top plate moved continuously downward to compact the sample by 60%. We defined potential contacts using general contact in explicit dynamic simulations, with contact properties set to hard contact in the forward direction and a tangential friction coefficient of 0.1. The loading velocity was meticulously chosen to ensure that the ratio of kinetic energy to internal energy remains below 1%, allowing us to disregard the influence of loading velocity. The axial stress is used to characterize the collapse strength of each step, either as plateau stress (in stable mode) or peak stress (in unstable mode). The compression modulus is defined by the
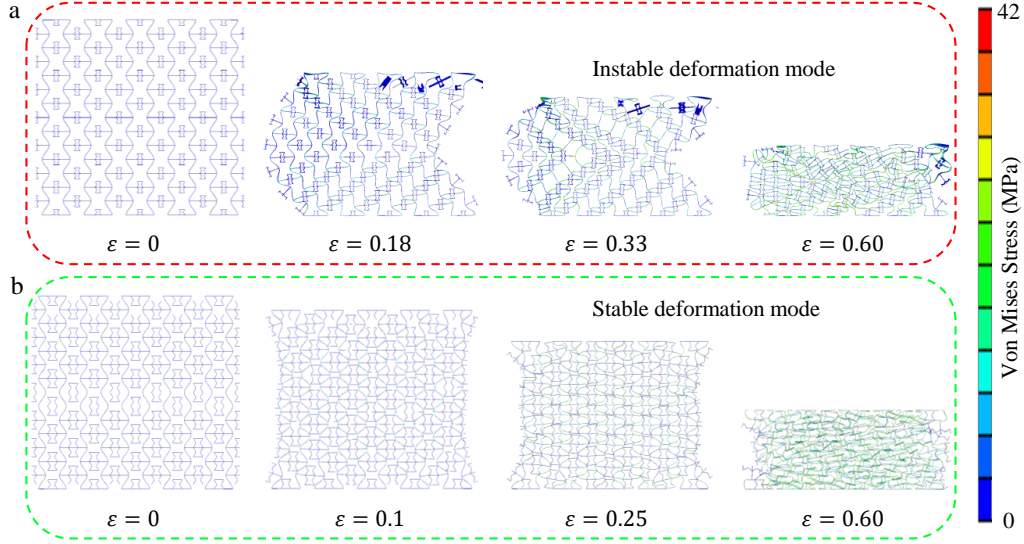
Figure 4: For relative densities below 0.1, the selected deformed frames for (a) S-1/5A are dominated by an unstable reconfigured mechanism, whereas (b) other multi-step configurations are governed by a stable reconfigured mechanism, with configuration S-1/3A considered in the illustration.

maximum tangent modulus in each step.

4.1. Large inelastic deformation response to uniaxial compression

Figure 3 illustrates the stress-strain response of auxetic structures with varying relative densities, as determined through numerical simulations. At a relative density of 0.05, the OA structure undergoes an initial elastic deformation, followed by a weakly nonlinear and progressively increasing behavior. Upon reaching the first peak stress of approximately 6 kPa, the OA structure experiences irreversible global instability, resulting in a weakly nonlinear decreasing response until densification occurs. This dominant mechanism remains consistent for OA with higher relative density. Similar deformation trends and stress-strain responses are evident in Fig. 5a and Fig. 3.

Regarding multi-step configurations, the deformation mechanisms and compressive response undergo significant changes influenced by both the inner structure and the relative density. Similarly, all multi-step configurations display an initial elastic behavior followed by a compression response that nearly plateaus, albeit with lower stress levels. As the applied strain progresses, all configurations transition into the second phase, and the stresses exhibit a noticeable trend of stepwise increase.

A larger size of the embedded microstructure leads to an earlier reconfiguration strain and a more stable reconfiguration path. For all relative densities, S-1/3A exhibits no noticeable buckling behavior (See Fig. 4b and Fig. 5d). The corresponding reconfigured strain is approximately 0.1. The compression response of these configurations increases gradually but persistently, which we attribute to the contact between the emended structures and the outer structures. In the case of configuration S-1/4A, global buckling occurs prior to the initiation of reconfiguration. However,
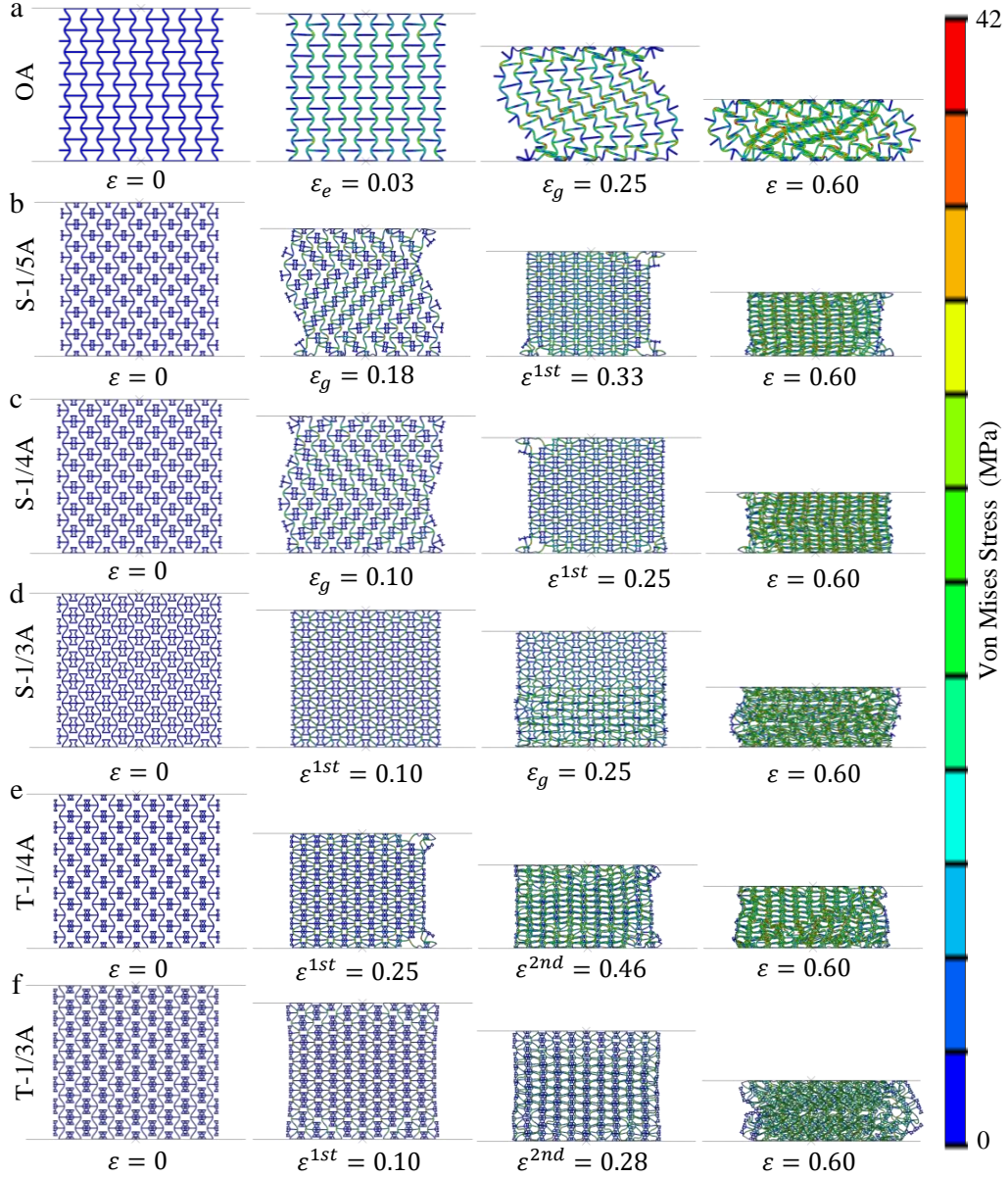
Figure 5: Large strain simulation results: deformation pattern of auxetic structures with a relative density of 0.2 under compression strains, encompassing stages such as the initial state, elastic deformation, first reconfiguration, second reconfiguration, global buckling, and the final state.

the rotating mechanism overcomes the buckling mechanism, leading to the reconfiguration of S-1/4A into a stable mode at an applied strain of approximately 0.25 (See Fig. 5c). The deformation is uniform, and the corresponding response remains almost constant. For configuration S-1/5, the game between the two mechanisms mainly depends on the relative density. When the relative

density is below 0.1, reconfiguration is primarily influenced by buckling, and the compression response is not significantly enhanced. Conversely, the opposite holds true for high relative density (See Fig. 4a and Fig. 5b). The corresponding reconfigured strain is approximately 0.33. Configurations T-1/3A and T-1/4 undergo two reconfigurations during the deformation process (See Fig. 5e and Fig. 5f). Their initial reconfiguration coincides with the strain level observed in their second-order counterparts. Notably, both the deformation process and the associated compression response demonstrate stability in the subsequent stage. The second reconfiguration strains for configurations T-1/3A and T-1/4 are recorded at 0.28 and 0.46, respectively. During the third step, the response of T-1/3A consistently demonstrates a distinctive plateau behavior across all relative density values. In contrast, T-1/4A exhibits either a continuously increasing nonlinear response at low relative density or an escalating nonlinear response followed by a peak stress at high relative density.

4.2. Effect of embedded structures on compression modulus

Figure 6a depicts comparison of relative elastic modulus obtained from numerical simulation for all configurations. For all configurations, the relative elastic modulus scale nonlinearly with relative density. The relative elastic modulus of OA and S-1/5A can be approximated by the nonlinear functions

$$E_{\text{OA}}/E_{\text{s}} = (1081\bar{\rho}^3 - 68.01\bar{\rho}^2 + 2.434\bar{\rho})/1000 \tag{10}$$

and

$$E_{\text{S-1/5A}}/E_{\text{s}} = (168\bar{\rho}^3 + 4.567\bar{\rho}^2 - 0.4278\bar{\rho})/1000. \tag{11}$$

The incorporation of embedded structures clearly reduces the elastic modulus of OA. Specifically, the elastic modulus of OA is nearly 4 times larger than that of S-1/5A. Moreover, the expected trend suggests a further decrease in elastic modulus with an increase in the size of the inner structure. Notably, S-1/3A exhibits an elastic modulus comparable to T-1/4A. Furthermore, the elastic modulus of T-1/3A is merely 1/20-th of that of OA, which is not easily attained even in bending-dominated structures and auxetics. This phenomenon arises from the observation that the thickness of the multistage structure, featuring distinct embedded microstructures, is smaller than that of the original structure at the same relative density. The ability to tailor the elastic modulus to any value lower than OA by adjusting the embedded structure is readily imaginable.

In Figure 6b, the variations in the high-order compression modulus for all multi-step auxetics are illustrated, with OA serving as the reference. Notably, it is observed that all high-order compression moduli are significantly higher than their corresponding first-order modulus, which we attribute to the influence of contacts in reconfiguration. Moreover, these increases are closely associated with the deformed stability of these multi-step auxetics and the ability of stretching-dominated reconfiguration to resist deformation. As the relative density drops below 0.1, all configurations exhibit a higher high-order compression modulus than OA, with the exception of S-1/5A and T-1/3A (2-order). S-1/5A is notable for its unstable reconfiguration process, whereas the reconfiguration of T-1/3A is comparatively more flexible than other configurations. At other relative densities, all configurations prove to be stiffer than OA, with T-1/3A (2-order) persisting as the weakest among them. Notably, S-1/5A experiences an increase to about 3.8 times that of OA, which we attribute to the change in deformation stability. T-1/3A (3-order) exhibits the highest stiffness, reaching approximately 4 to 5 times that of OA.
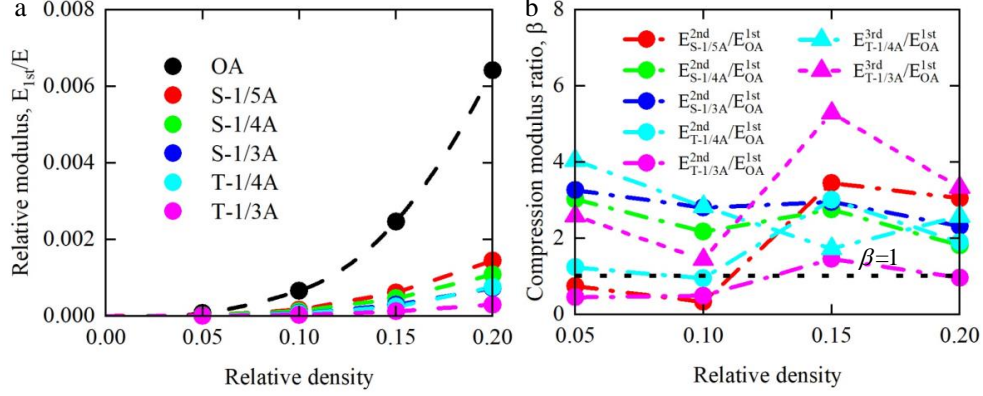
12

Figure 6: (a) Variations in the relative Young's modulus across different configurations as a function of relative density evolution. Notably, the elastic modulus of OA surpasses that of other configurations significantly. (b) Relative ratios of high-order compression modulus in multi-step configurations to the Young's modulus of the base OA for selected relative densities. All high-order compression moduli are significantly higher than their corresponding first-order modulus.

4.3. Effect of embedded structures on compression strength

Figure 7a illustrates the variations in relative strength across different relative densities for all configurations. Similar to Young's modulus, the first-order relative strength is nonlinear with relative density. The relative compression strength of OA and S-1/5A can also be approximated by the nonlinear functions

$$\sigma_{\text{OA}}/\sigma_s = (1531\bar{\rho}^3 - 43.03\bar{\rho}^2 + 6.958\bar{\rho})/1000 \tag{12}$$

and

$$\sigma_{\text{S}-1/5\text{A}}/\sigma_s = (-70.4\bar{\rho}^3 + 104.9\bar{\rho}^2 - 3.767\bar{\rho})/1000. \tag{13}$$

For the same reasons as with Young's modulus, the first-order relative strength decreases with order or scale factor. The relative strength of S-1/5A is nearly a quarter of that of OA. For all relative densities, the ratio of OA to T-1/3A can extend to a significant value of 14.9. This remarkably low strength and stiffness renders it conducive to reusability, even when employed with brittle base materials.

In Figure 7b, the first-order compression strength of OA is contrasted with the high-order compression strength of other multi-step auxetics. Observations reveal that 3rd order configurations consistently exhibit the lowest strength levels, as they fail to fully utilize every part in the second step. Configuration T-1/3A displays the lowest compression strength, registering absolute values approximately 60% of OA. Concurrently, the compression strength ratio of T-1/4A fluctuates around 1. Configurations S-1/4A and S-1/3 are noted to exhibit a moderate level of compression strength. Notably, the compression strength ratio of S-1/5A hovers around 1 for relative densities below 0.1, but shifts to around 2 for relative densities exceeding 0.1. This serves as additional evidence of the transition of S-1/5A from an unstable to a stable state. As the deformation advances into the third phase, the 3rd order configurations undergo a reconfiguration to attain the final stage, characterized by an ultra-strong state. Thus T-1/4A exhibits the highest compression strength, reaching approximately 4 to 6 times that of OA.
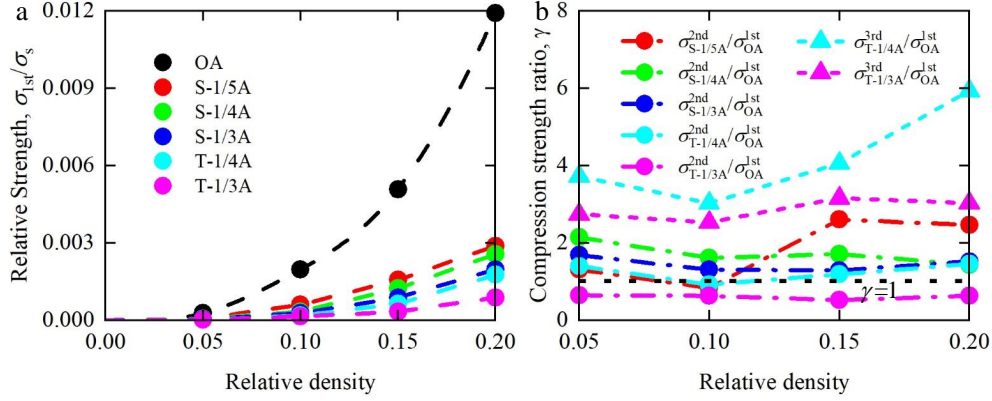
13

Figure 7: (a) Evolution of the relative compression strength as a function of relative density, revealing a consistent decrease in first-order relative strength with increasing order or scale factor. (b) Ratios between high-order compression strength of multi-step auxetics and first-order compression strength of OA at specific relative densities. Notably, most configurations exhibit higher high-order compression strength than OA.

4.4. Effect of embedded structures on Poisson's ratio

Figure 8 illustrates the variation of Poisson's ratio with strain, derived from numerical simulations for all configurations at four distinct relative densities. In general, second-order auxetics exhibit nearly the same Poisson's ratios as third-order auxetics, primarily owing to the almost identical thickness of the outer structure. For all relative densities, all configurations exhibit nearly the same initial negative Poisson's ratio values of approximately −1, followed by a consistent and gradually increasing trend. For configurations OA and S-1/5A ($\overline{\rho} \leq 0.1$), the auxetic behavior persists until irreversible global buckling occurs at an applied strain of approximately 0.05. The ultimate Poisson's ratio ranges from −0.87 to −0.65 across different relative densities. In high relative density scenarios, the deformation mode undergoes a substantial transformation in configuration S-1/5A upon the loss of stability.

The contraction of the unit cell slows down and Poisson's ratio experiences a rapid increase, reaching a positive value of either 0.36 or 0.7. Continuing the loading process amplifies the degree of instability, leading to a reversal in Poisson's ratio back to a negative value. At an applied strain of approximately 0.18, the inner structure begins to make contact with the outer structure in an asymmetrical manner, as depicted in Figure 9d. Subsequently, the structure undergoes reconfiguration, transitioning to another stable stage at a strain of about 0.2. This transition coincides with a rapid decrease in Poisson's ratio, reaching its peak value. Upon reconfiguration, Poisson's ratio undergoes a sudden jump from the peak value to −1. As the applied strain continues to increase thereafter, Poisson's ratio displays a slow and gradual ascent, ultimately reaching 0. The stabilization of Poisson's ratio at approximately 0 is attributed to the occurrence of layer-by-layer collapse. For configurations S-1/4A and T-1/4A, local buckling manifests in a more gradual and subdued manner. Notably, the slopes of their Poisson's curves are evidently smaller compared to configuration S-1/5A. Similarly, configurations S-1/4A and T-1/4A exhibit a comparable yet more moderate jumping behavior compared to configuration S-1/5A. However, it is important to note that the deformation mode for each extreme point remains distinct. In the first two extreme points, the inner structure comes into contact with the outer structure on one side and on two sides, respectively. Reconfiguration is completed at the third extreme point, and the
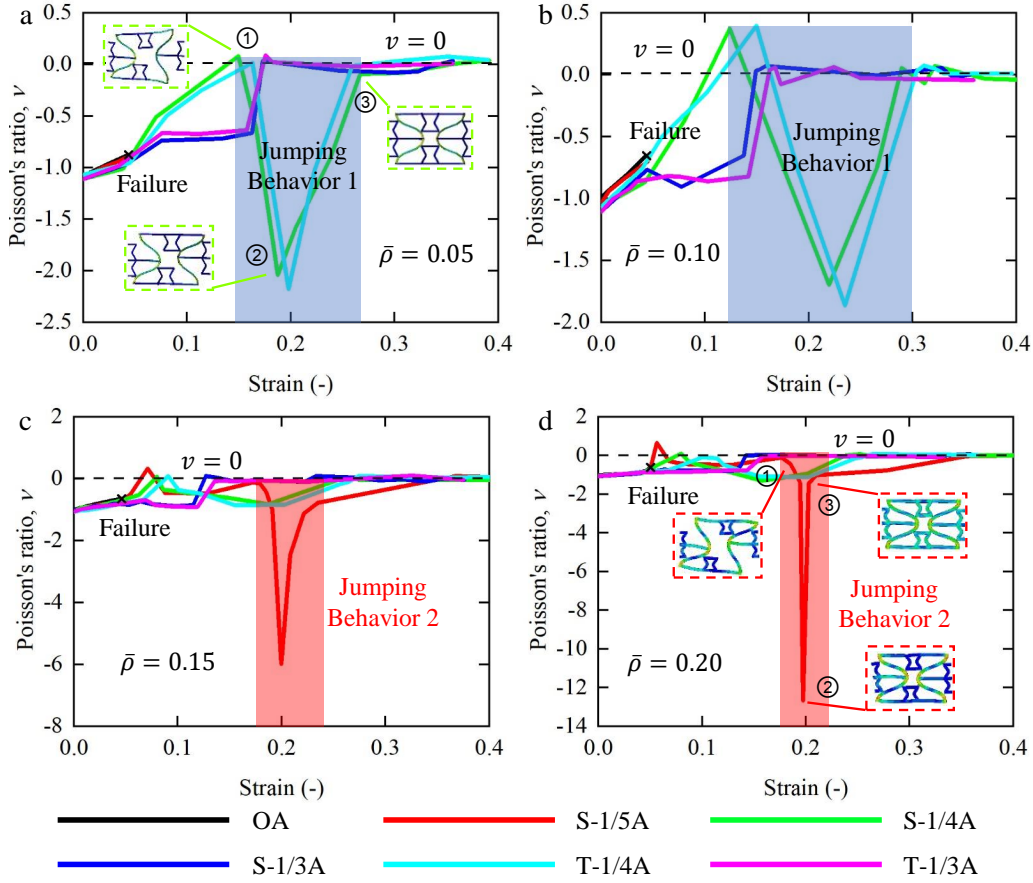
14

Figure 8: Evolution of the Poisson's ratios as a function of compressive strain for all relative densities. In the case of configurations OA, the auxetic behavior persists until irreversible global buckling takes place. In contrast, other high-order configurations with jumping behavior span a wide range of auxetic behavior.

corresponding Poisson's ratio then stabilizes at around 0. For configurations S-1/3A and T-1/3A, their distinctive structural properties effectively suppress the occurrence of both local buckling and global buckling. The ensuing deformation in these configurations is uniform, enabling a stable negative plateau during reconfiguration. The ensuing deformation in these configurations is uniform, resulting in a stable negative Poisson's ratio plateau during the reconfiguration process. Until the configurations are reconfigured and undergo layer-by-layer buckling, the Poisson's ratio increases rapidly to 0 and then stabilizes near 0. Consequently, the proposed multi-step mechanism extends the duration of auxetic behavior, providing more opportunities for tailoring mechanical properties.

4.5. Effect of embedded structures on energy absorption

For energy absorbing materials, specific absorption energy (SEA) is typically characterized as the work accomplished through uniaxial compression, consistently evaluated up to a defined
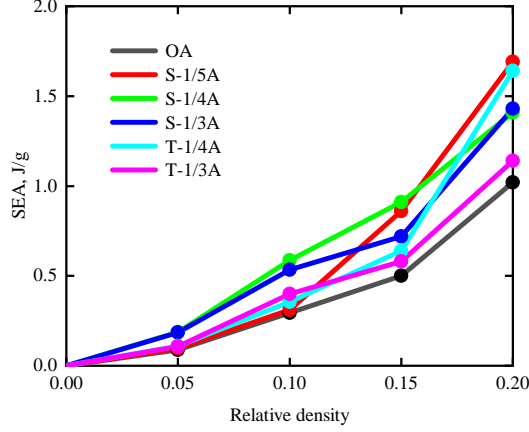
15

Figure 9: Evolution of SEA for all configurations as a function of relative density. Multi-step auxetics outperform conventional auxetics for strain energy absorption.

strain, here set at 0.6, per gram of mass as

$$\text{SEA} = \frac{V \int_0^{0.6} \sigma d\varepsilon}{M} \tag{14}$$

Figure 9 illustrates the evolution of SEA across diverse configurations with respect to changing relative densities. Notably, it becomes evident that multi-step auxetics exhibit a superior capacity for absorbing strain energy compared to conventional auxetics. When the relative density does not exceed 0.1, configurations S-1/4A and S-1/3A exhibit optimal performance in SEA, surpassing OA by almost 2.1 times. This superiority can be attributed to either a commendably stable nonlinear response or a recoverable buckling mechanism. At this stage, these two deformation mechanisms are mutually compatible. At a relative density of 0.15, S-1/4A processes the highest SEA of about 0.91 J/g. Intriguingly, the energy absorption capacity of S-1/5A shifts from the lowest to the second-best level. Furthermore, at a relative density of 0.2, the SEA values of S-1/5A stand out favorably when compared to other configurations, underscoring the success of the recoverable buckling mechanism. Notably, the energy-absorbing capacity of T-1/4A undergoes a significant enhancement, as anticipated for high relative density.

5. Experimental results and discussion

Figure 10a and c showcases the deformation frames of the OA structure, featuring main load-bearing components intricately shaped in a sinusoidal manner to mitigate stress concentrations. In the course of compression along the *y* axis (refer to Video S1), the structural deformation can be broadly categorized into three stages: elastic deformation, global instability, and densification. Initially, the structure undergoes overall inward shrinkage, attributed to its inherent negative Poisson's ratio property, constituting a phase of linear elastic deformation. The structure exhibits a linear response with increasing stress during this stage, as depicted in Figure 10a and b. Upon reaching the initial peak stress of approximately 0.35 MPa, the structure gradually loses stability and protrudes outward to the right side in the mid-plane. Correspondingly, the stress plateaus
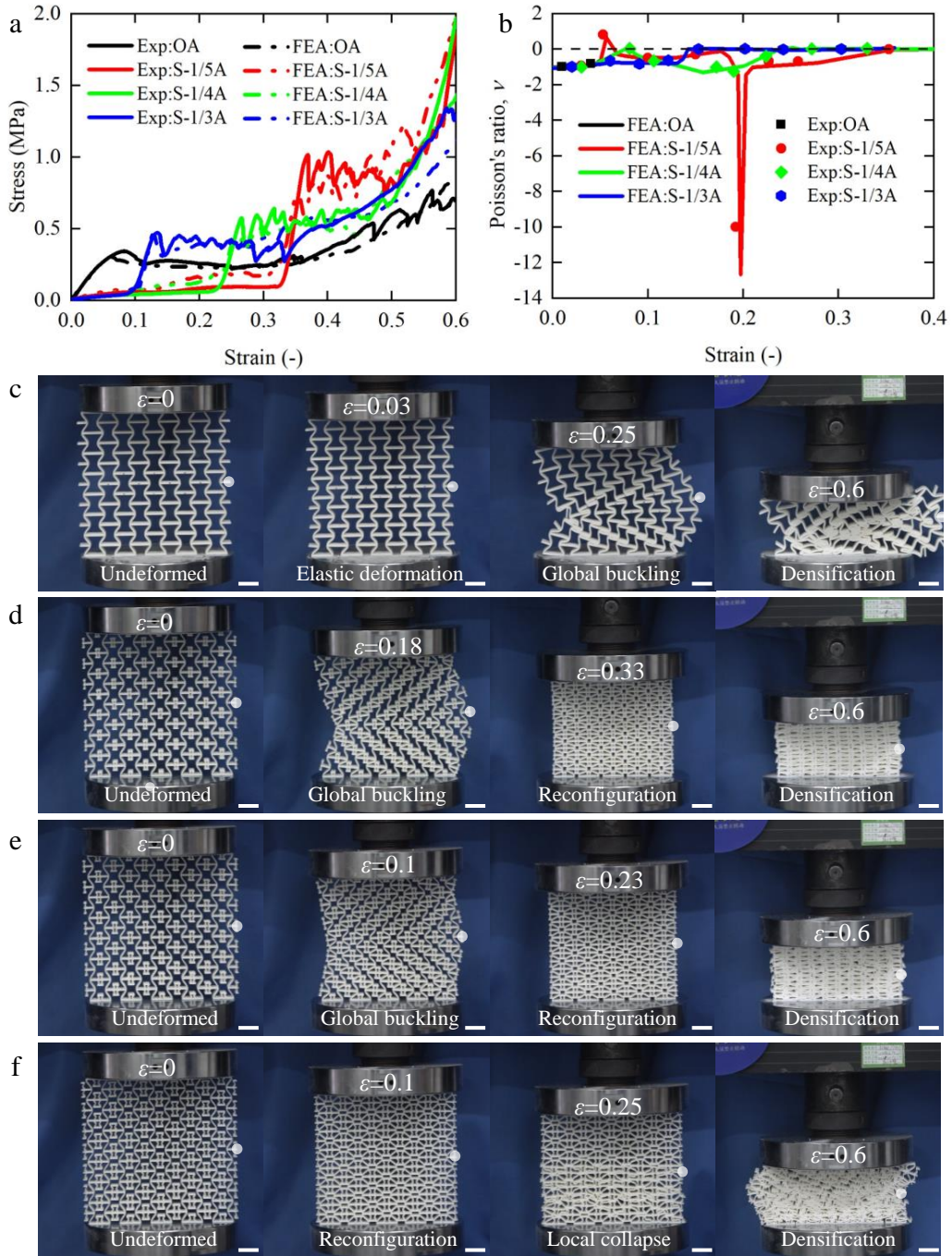
Figure 10: Compression experiments with auxetics samples fabricated by 3D printing technology. (a) Stress-strain curves and (b) Poisson's ratio for both first-order and second-order auxetics are presented, based on data derived from both experimental observations and simulations. These results, depicted for a relative density of approximately 0.2, demonstrate a close agreement between experimental findings and numerical predictions. (d)-(f) The acquired frames corresponding to compression tests on samples reveal distinct stages, encompassing the initial state, inelastic buckling, subsequent reconfiguration, and the phase of substantial compression up to the maximum applied strain. All scale bars are 2 cm long.

after a slight decrease. As the deformation progresses further, the structure gradually undergoes densification, accompanied by a slow increase in stress.

Figures 10d and e present the deformation frames of the second-order auxetic structures S-1/5A and S-1/4A, showcasing behavior distinct from what was observed for OA. Intriguingly, subtle variations in the size of the embedded micro-structures (1/5 and 1/4) result in distinct behavior of the system during deformation, as evidenced in Videos S2 and S3. The deformation process of these structures is broadly characterized into five stages with two distinct steps: elastic deformation, global instability, instability recovery, layer-by-layer buckling, and densification. Initially, the structures experience elastic deformation, with stress gradually increasing until reaching approximately 0.05 MPa. The exceptionally low stress levels observed, unmatched in structures dominated by either bending or stretching with equal relative density, highlight their compelling potential for impact resistance and body protection. Similar to the OA structure, structures S-1/5A and S-1/4A also experience global buckling. The notable difference lies in the recoverability of the instability, stemming from high resistance of the embedded structure to rotating force. This recoverability persists as the applied strain continues, leading to the formation of another stable stage, and the stress value tends to plateau. It becomes evident that the transform strain is primarily determined by the size of the embedded structure: the larger the micro-structure embedded, the smaller the transform strain. Once reconstruction is completed, the stress value increases rapidly, marking the transition into the second step.

After reaching the first peak stress, structures S-1/5A and S-1/4A undergo layer-by-layer collapse in a nearly stable mode, accompanied by small-amplitude oscillations in stress. The first peak of S-1/4A has an amplitude of about 1.01 MPa, nearly twice that of S-1/5A, and almost three times that of OA. This may be attributed to the regenerated stretching-dominated structure making more efficient use of micro-components in terms of loading support. When the applied strain exceeds 0.5, structures S-1/5A and S-1/4A initiate the densification process. Figure 10f presents the deformation frames of the S-1/3A configuration. In contrast to other second-order auxetics, S-1/3A showcases a stable and uniform deformation behavior (See Movie S4) along with an improved second step compression response. Figure 11 presents stress-strain curves and deformation frames of T-1/4A and T-1/3A (See Movies S5 and S6). In the initial two steps, both configurations exhibit a similar deformation and compression response akin to their lower-order counterpart. With the ongoing applied strain, the second reconstruction occurs through the contact between the third-order inner structure and the second-order inner structure. Ultimately, the stress value decreases, indicative of the overall instability of the structure. For all configurations, both experimental and numerical compressive responses exhibit similar trends. Experimental results are in good agreement with numerical predictions regarding compression modulus, compression, Poisson's ratio, and SEA, as outlined in Table S1. Prediction errors may be attributed to printing errors, imperfections and flaws.

To acquire a deeper understanding of the overall instability of the structures, displacements at the right middle position of the structure were individually measured for samples OA, S-1/5A, S-1/4A, and S-1/3A, as illustrated in Fig. 12. In the initial stages of deformation, the labeled positions of all configurations follow the same displacement path, progressing along the negative direction of x owing to the auxetic behavior. When the vertical displacement reaches 5 mm, global buckling becomes dominant in configurations expect for S-1/3A, leading to the labeled points to shift along the positive direction of x. Unlike OA, the labeled points of S-1/5A and S-1/4A move along the negative x direction for the second time when the structure begins to recover from an unstable state to a stable state. Upon reconstruction of the structure, the labeled points cease to move along the x direction and instead move solely along the negative y
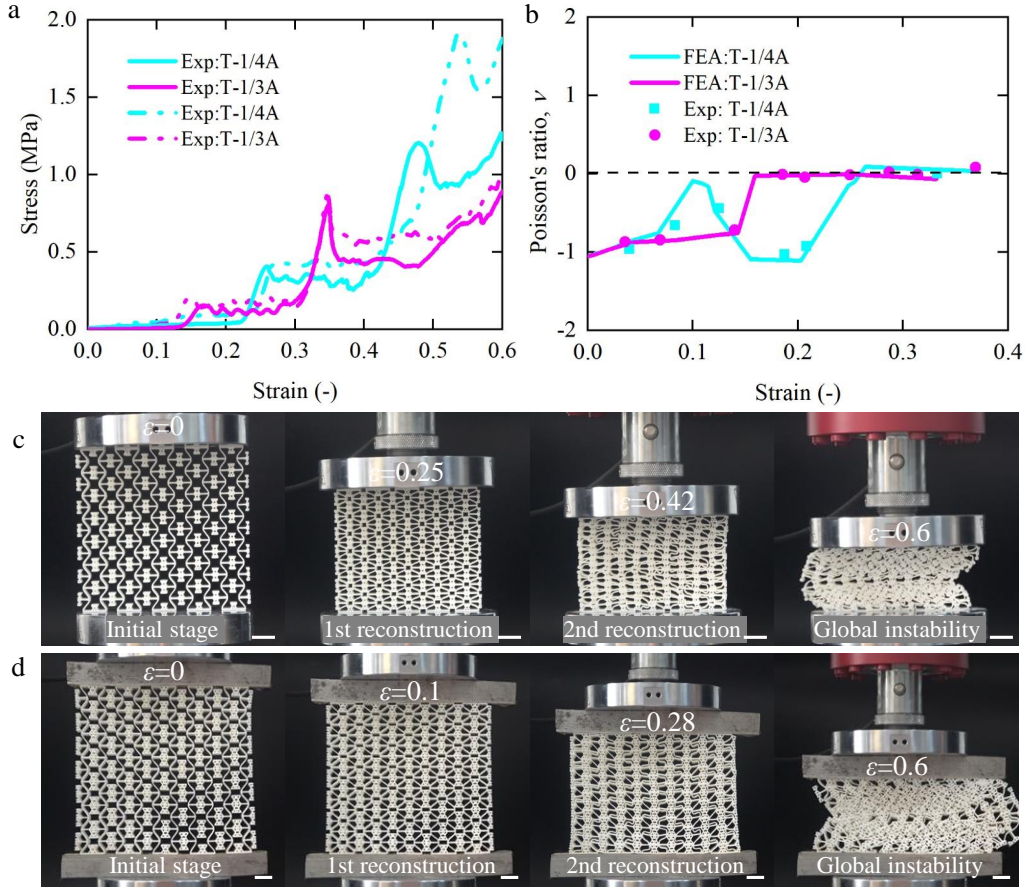
Figure 11: Uniaxial compression experiments are conducted on T-1/4A and T-1/3A samples with a relative density of 0.2. The results are presented as follows: (a) Engineering stress-strain curves and (b) Poisson's ratio for both T-1/4A and T-1/3A. Notably, simulation results exhibit good agreement with experimental data. Additionally, (c) showcases photographs of the deformed T-1/4A sample during compression, while (d) provides a visual representation of the deformed T-1/3A sample under compression. All scale bars are 2 cm long.

direction. The integrated microstructure, as a cohesive unit, profoundly shapes the deformation pattern of the system, leading to diverse levels of stable or unstable behavior. In its entirety, the amalgamation of tailored nonlinear response, multi-phase mechanical properties, and augmented energy absorption positions the proposed auxetics as a promising choice for applications in multi-stage load-bearing and impact energy absorption.

6. Conclusion

Here, we have presented a novel strategy for designing and fabricating a class of auxetic metamaterial characterized by an extended duration of auxetic behavior, regulated instability, and improved energy absorption. The effective mechanical properties have been investigated both numerically and experimentally. The results demonstrate that the deformation mechanism
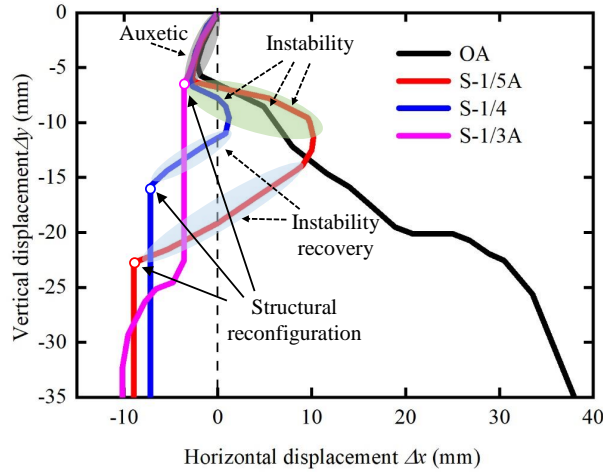
Figure 12: Displacements at the designated position on the right side of the structure correspond to movement in the positive direction to the right and upward in the horizontal and vertical orientations, respectively.

and compression response of the proposed multi-step auxetics are strongly influenced by the reduction factor and orders of the inner structure. Notably, nonlinear buckling behavior can be completely suppressed when the reduction factor is 1/3. Moreover, we are intrigued to observe that the inclusion of embedded microstructures can restore stable deformation, even in the presence of significant initial instability, particularly with reduction factors of 1/4 and 1/5. Additionally, at a relative density of 0.2, the SEA of sample S-1/5A stands out favorably compared to other configurations, highlighting the success of the recoverable buckling mechanism. Meanwhile, the multi-step auxetics generally exhibit multi-phase compression modulus and strength. Specifically, their low-order modulus and strength are only a fraction of those of OA, whereas their high-order compression properties are several times greater than those of OA. The exceptional stress levels observed, unmatched in structures dominated by either bending or stretching with equal relative density, highlight their compelling potential for impact resistance and body protection.

Declaration of Competing Interest

The authors declare that they have no known competing financial interests or personal relationships that could have appeared to influence the work reported in this paper.

CRediT authorship contribution statement

P.Y. and X.C. designed research; P.Y, P.Z, Q.J., F.Y., X.T., X.C. performed research; P.Y. analyzed data; P.Y., X.C., H.T., V.L. and M.K. discussed the results and wrote the paper.

Acknowledgments

References

[1] C. Coulais, A. Sabbadini, F. Vink, M. van Hecke, Multi-step self-guided pathways for shape-changing metamaterials, Nature 561 (7724) (2018) 512–515.

[2] B. Florijn, C. Coulais, M. van Hecke, Programmable mechanical metamaterials, Physical Review Letters 113 (17) (2014) 175503.

[3] C. Coulais, D. Sounas, A. Alu, Static non-reciprocity in mechanical metamaterials, Nature 542 (7642) (2017) 461–464.

[4] W. Gao, J. Kang, G. Wang, H. Ma, X. Chen, M. Kadic, V. Laude, H. Tan, Y. Wang, Programmable and variable-stiffness robotic skins for pneumatic actuation, Advanced Intelligent Systems (2023) 2300285.

[5] T. Bückmann, R. Schittny, M. Thiel, M. Kadic, G. W. Milton, M. Wegener, On three-dimensional dilational elastic metamaterials, New Journal of Physics 16 (3) (2014) 033032.

[6] T. Bückmann, N. Stenger, M. Kadic, J. Kaschke, A. Frölich, T. Kennerknecht, C. Eberl, M. Thiel, M. Wegener, Tailored 3d mechanical metamaterials made by dip-in direct-laser-writing optical lithography, Advanced Materials 24 (20) (2012) 2710–2714.

[7] X. Chen, J. Moughames, Q. Ji, J. A. Iglesias Martínez, H. Tan, S. Adrar, N. Laforge, J.-M. Cote, S. Euphrasie, G. Ulliac, et al., Optimal isotropic, reusable truss lattice material with near-zero poisson's ratio, Extreme Mechanics Letters 41 (2020) 101048.

[8] K. K. Dudek, J. A. Iglesias Martínez, G. Ulliac, L. Hirsinger, L. Wang, V. Laude, M. Kadic, Micro-scale mechanical metamaterial with a controllable transition in the poisson's ratio and band gap formation, Advanced Materials (2023) 2210993.

[9] L. Wang, G. Ulliac, B. Wang, J. A. Iglesias Martínez, K. K. Dudek, V. Laude, M. Kadic, 3d auxetic metamaterials with elastically-stable continuous phase transition, Advanced Science 9 (34) (2022) 2204721.

[10] X. Chen, Q. Ji, J. Wei, H. Tan, J. Yu, P. Zhang, V. Laude, M. Kadic, Light-weight shell-lattice metamaterials for mechanical shock absorption, International Journal of Mechanical Sciences 169 (2020) 105288.

[11] S. C. Han, J. W. Lee, K. Kang, A new type of low density material: Shellular, Advanced Materials 27 (37) (2015) 5506–5511.

[12] X. Chen, Q. Ji, J. A. Iglesias Martinez, H. Tan, G. Ulliac, V. Laude, M. Kadic, Closed tubular mechanical metamaterial as lightweight load-bearing structure and energy absorber, Journal of the Mechanics and Physics of Solids 167 (2022) 104957.

[13] J. B. Berger, H. N. G. Wadley, R. M. McMeeking, Mechanical metamaterials at the theoretical limit of isotropic elastic stiffness, Nature 543 (7646) (2017) 533–537.

[14] T. Tancogne-Dejean, M. Diamantopoulou, M. B. Gorji, C. Bonatti, D. Mohr, 3d plate-lattices: an emerging class of low-density metamaterial exhibiting optimal isotropic stiffness, Advanced Materials 30 (45) (2018) 1803334.

[15] X. Chen, J. Moughames, Q. Ji, J. A. Iglesias Martínez, H. Tan, G. Ulliac, V. Laude, M. Kadic, 3d lightweight mechanical metamaterial with nearly isotropic inelastic large deformation response, Journal of the Mechanics and Physics of Solids 169 (2022) 105057.

[16] P. Zhang, P. Yu, R. Zhang, X. Chen, H. Tan, Grid octet truss lattice materials for energy absorption, International Journal of Mechanical Sciences 259 (2023) 108616.

[17] B. Jiang, X. Chen, J. Yu, Y. Zhao, Z. Xie, H. Tan, Energy-absorbing properties of thin-walled square tubes filled with hollow spheres, Thin-Walled Structures 180 (2022) 109765.

[18] S. Zhu, X. Tan, B. Wang, S. Chen, J. Hu, L. Ma, L. Wu, Bio-inspired multistable metamaterials with reusable large deformation and ultra-high mechanical performance, Extreme Mechanics Letters 32 (2019) 100548.

[19] T. Frenzel, C. Findeisen, M. Kadic, P. Gumbsch, M. Wegener, Tailored buckling microlattices as reusable lightweight shock absorbers, Advanced Materials 28 (28) (2016) 5865–5870.

[20] H. Yang, L. Ma, 1d to 3d multi-stable architected materials with zero poisson's ratio and controllable thermal expansion, Materials & Design 188 (2020) 108430.

[21] X. Chen, H. Tan, An effective length model for octet lattice, International Journal of Mechanical Sciences 140 (2018) 279–287.

[22] D. Jang, L. R. Meza, F. Greer, J. R. Greer, Fabrication and deformation of three-dimensional hollow ceramic nanostructures, Nature Materials 12 (10) (2013) 893–898.

[23] X. Zheng, H. Lee, T. H. Weisgraber, M. Shusteff, J. DeOtte, E. B. Duoss, J. D. Kuntz, M. M. Biener, Q. Ge, J. A. Jackson, et al., Ultralight, ultrastiff mechanical metamaterials, Science 344 (6190) (2014) 1373–1377.

[24] X. Ren, J. Shen, P. Tran, T. D. Ngo, Y. M. Xie, Auxetic nail: Design and experimental study, Composite Structures 184 (2018) 288–298.

[25] C. Luo, C. Z. Han, X. Y. Zhang, X. G. Zhang, X. Ren, Y. M. Xie, Design, manufacturing and applications of auxetic tubular structures: A review, Thin-Walled Structures 163 (2021) 107682.

[26] X.-T. Wang, B. Wang, X.-W. Li, L. Ma, Mechanical properties of 3d re-entrant auxetic cellular structures, International Journal of Mechanical Sciences 131 (2017) 396–407.

[27] K. E. Evans, A. Alderson, Auxetic materials: functional materials and structures from lateral thinking!, Advanced materials 12 (9) (2000) 617–628.

[28] J. B. Choi, R. S. Lakes, Fracture toughness of re-entrant foam materials with a negative poisson's ratio: experiment and analysis, International Journal of fracture 80 (1996) 73–83.

[29] X.-T. Wang, X.-W. Li, L. Ma, Interlocking assembled 3d auxetic cellular structures, Materials & Design 99 (2016) 467–476.

[30] X.-T. Wang, B. Wang, Z.-H. Wen, L. Ma, Fabrication and mechanical properties of cfrp composite three-dimensional double-arrow-head auxetic structures, Composites Science and Technology 164 (2018) 92–102.

[31] T. Frenzel, M. Kadic, M. Wegener, Three-dimensional mechanical metamaterials with a twist, Science 358 (6366) (2017) 1072–1074.

[32] T. Frenzel, J. Köpfler, E. Jung, M. Kadic, M. Wegener, Ultrasound experiments on acoustical activity in chiral mechanical metamaterials, Nature communications 10 (1) (2019) 3384.

[33] X. Ren, R. Das, P. Tran, T. D. Ngo, Y. M. Xie, Auxetic metamaterials and structures: a review, Smart materials and structures 27 (2) (2018) 023001.

[34] W. Jiang, X. G. Zhang, D. Han, L. Wang, W. Q. Chen, Y. M. Xie, X. Ren, Experimental and numerical analysis of a novel assembled auxetic structure with two-stage programmable mechanical properties, Thin-Walled Structures 185 (2023) 110555.

[35] R. D. Vocke III, C. S. Kothera, B. K. Woods, N. M. Wereley, Development and testing of a span-extending morphing wing, Journal of Intelligent Material Systems and Structures 22 (9) (2011) 879–890.

[36] M. A. Wagner, T. S. Lumpe, T. Chen, K. Shea, Programmable, active lattice structures: Unifying stretch-dominated and bending-dominated topologies, Extreme Mechanics Letters 29 (2019) 100461.

[37] X. Huang, W. Guo, S. Liu, Y. Li, Y. Qiu, H. Fang, G. Yang, K. Zhu, Z. Yin, Z. Li, et al., Flexible mechanical meta-materials enabled electronic skin for real-time detection of unstable grasping in robotic manipulation, Advanced Functional Materials 32 (23) (2022) 2109109.

[38] Y. Jiang, Z. Liu, N. Matsuhisa, D. Qi, W. R. Leow, H. Yang, J. Yu, G. Chen, Y. Liu, C. Wan, et al., Auxetic mechanical metamaterials to enhance sensitivity of stretchable strain sensors, Advanced Materials 30 (12) (2018) 1706589.

[39] R. Lakes, Foam structures with a negative poisson's ratio, Science 235 (4792) (1987) 1038–1040.

[40] K. E. Evans, Auxetic polymers: a new range of materials, Endeavour 15 (4) (1991) 170–174.

[41] J. N. Grima, K. E. Evans, Auxetic behavior from rotating squares, Journal of materials science letters 19 (2000) 1563–1565.

[42] J. N. Grima, R. Jackson, A. Alderson, K. E. Evans, Do zeolites have negative poisson's ratios?, Advanced Materials 12 (24) (2000) 1912–1918.

[43] J. N. Grima, A. Alderson, K. E. Evans, Negative poisson's ratios from rotating rectangles, Cmst 10 (2) (2004) 137–145.

[44] J. N. Grima, K. E. Evans, Auxetic behavior from rotating triangles, Journal of materials science 41 (10) (2006) 3193–3196.

[45] J. N. Grima, E. Manicaro, D. Attard, Auxetic behaviour from connected different-sized squares and rectangles, Proceedings of the royal society A: mathematical, physical and engineering sciences 467 (2126) (2011) 439–458.

[46] L. J. Gibson, Cellular solids, Mrs Bulletin 28 (4) (2003) 270–274.

[47] K. E. Evans, M. Nkansah, I. Hutchinson, Auxetic foams: modelling negative poisson's ratios, Acta metallurgica et materialia 42 (4) (1994) 1289–1294.

[48] H. Yang, L. Ma, Design and characterization of axisymmetric auxetic metamaterials, Composite Structures 249 (2020) 112560.

[49] R. Lakes, Deformation mechanisms in negative poisson's ratio materials: structural aspects, Journal of materials science 26 (1991) 2287–2292.

[50] D. Prall, R. Lakes, Properties of a chiral honeycomb with a poisson's ratio of—1, International Journal of Mechanical Sciences 39 (3) (1997) 305–314.

[51] C. S. Ha, M. E. Plesha, R. S. Lakes, Chiral three-dimensional lattices with tunable poisson's ratio, Smart Materials and Structures 25 (5) (2016) 054005.

[52] K. K. Dudek, L. Mizzi, J. A. Iglesias Martínez, A. Spaggiari, G. Ulliac, R. Gatt, J. N. Grima, V. Laude, M. Kadic, Micro-scale graded mechanical metamaterials exhibiting versatile poisson's ratio, Composite Structures 319 (2023) 117151.

[53] J. N. Grima, R. Gatt, Perforated sheets exhibiting negative poisson's ratios, Advanced engineering materials 12 (6) (2010) 460–464.

[54] J. N. Grima, L. Mizzi, K. M. Azzopardi, R. Gatt, Auxetic perforated mechanical metamaterials with randomly oriented cuts, Advanced materials 28 (2) (2016) 385–389.

[55] S. Babaee, J. Shim, J. C. Weaver, E. R. Chen, N. Patel, K. Bertoldi, 3d soft metamaterials with negative poisson's ratio, Advanced Materials 25 (36) (2013) 5044–5049.

[56] C. W. Smith, J. N. Grima, K. Evans, A novel mechanism for generating auxetic behaviour in reticulated foams: missing rib foam model, Acta materialia 48 (17) (2000) 4349–4356.

[57] S. Yuan, F. Shen, J. Bai, C. K. Chua, J. Wei, K. Zhou, 3d soft auxetic lattice structures fabricated by selective laser sintering: Tpu powder evaluation and process optimization, Materials & Design 120 (2017) 317–327.

[58] I. Masters, K. Evans, Models for the elastic deformation of honeycombs, Composite structures 35 (4) (1996) 403–422.

[59] I. Berinskii, Elastic networks to model auxetic properties of cellular materials, International Journal of Mechanical Sciences 115 (2016) 481–488.

[60] F. Xu, K. Yu, L. Hua, In-plane dynamic response and multi-objective optimization of negative poisson's ratio (npr) honeycomb structures with sinusoidal curve, Composite Structures 269 (2021) 114018.

[61] X.-L. Peng, S. Bargmann, A novel hybrid-honeycomb structure: Enhanced stiffness, tunable auxeticity and negative thermal expansion, International Journal of Mechanical Sciences 190 (2021) 106021.

[62] J. Zhang, G. Lu, D. Ruan, Z. Wang, Tensile behavior of an auxetic structure: Analytical modeling and finite element analysis, International Journal of Mechanical Sciences 136 (2018) 143–154.

[63] H. Niknam, A. Akbarzadeh, In-plane and out-of-plane buckling of architected cellular plates: Numerical and experimental study, Composite Structures 206 (2018) 739–749.

[64] W. Wu, P. Liu, Z. Kang, A novel mechanical metamaterial with simultaneous stretching-and compression-expanding property, Materials & Design 208 (2021) 109930.

[65] A.-E. Viard, J. Dirrenberger, S. Forest, Propagating material instabilities in planar architectured materials, International Journal of Solids and Structures 202 (2020) 532–551.

[66] J. Li, N. Arora, S. Rudykh, Elastic instabilities, microstructure transformations, and pattern formations in soft materials, Current Opinion in Solid State and Materials Science 25 (2) (2021) 100898.

[67] X. Cheng, Y. Zhang, X. Ren, D. Han, W. Jiang, X. G. Zhang, H. C. Luo, Y. M. Xie, Design and mechanical characteristics of auxetic metamaterial with tunable stiffness, International Journal of Mechanical Sciences 223 (2022) 107286.

[68] X. Y. Zhang, X. Ren, Y. Zhang, Y. M. Xie, A novel auxetic metamaterial with enhanced mechanical properties and tunable auxeticity, Thin-Walled Structures 174 (2022) 109162.

[69] H. Jiang, Y. Ren, Q. Jin, G. Zhu, Y. Hu, F. Cheng, Crashworthiness of novel concentric auxetic reentrant honeycomb with negative poisson's ratio biologically inspired by coconut palm, Thin-Walled Structures 154 (2020) 106911.

[70] J. Feng, Q. Liang, Y. Dou, J. He, Y. Wu, T. Chen, Higher stiffness hierarchical embedded strengthening honeycomb metastructure with small negative poisson's ratio reduction, Thin-Walled Structures 179 (2022) 109561.

[71] X. Li, R. Fan, Z. Fan, Y. Lu, Programmable mechanical metamaterials based on hierarchical rotating structures, International Journal of Solids and Structures 216 (2021) 145–155.

[72] H. Lu, X. Wang, T. Chen, Design and quasi-static responses of a hierarchical negative poisson's ratio structure with three plateau stages and three-step deformation, Composite Structures 291 (2022) 115591.

[73] L. P. Hyatt, R. L. Harne, Rapid pneumatic control of bimodal, hierarchical mechanical metamaterials, Advanced Engineering Materials 24 (7) (2022) 2101375.

[74] Z. Meng, M. Liu, Y. Zhang, C. Q. Chen, Multi-step deformation mechanical metamaterials, Journal of the Mechanics and Physics of Solids 144 (2020) 104095.

[75] F. Jiang, S. Yang, C. Qi, H.-T. Liu, Two plateau characteristics of re-entrant auxetic honeycomb along concave direction, Thin-Walled Structures 179 (2022) 109665.

[76] C. Eberl, R. Thompson, D. Gianola, S. Bundschuh, Digital image correlation and tracking with matlab, Matlab Central file exchange (2006).